Fast multimodel finite-difference controlled-source electromagnetic simulations based on a Schur complement approach

Piyoosh Jaysaval[1], Daniil Shantsev[2], and Sébastien de la Kethulle de Ryhove[2]

ABSTRACT

We have developed an efficient numerical scheme for fast multimodel 3D electromagnetic simulations by applying a Schur complement approach to a frequency-domain finite-difference method. The scheme is based on direct solvers and developed with constrained inversion algorithms in view. Such algorithms normally need many forward modeling jobs with different resistivities for the target zone and/or background formation. We geometrically divide the computational domain into two subdomains: an anomalous subdomain, the resistivities of which were permitted to change, and a background subdomain, having fixed resistivities. The system matrix is partially factorized by precomputing a Schur complement to eliminate unknowns associated with the background subdomain. The Schur complement system is then solved to compute fields inside the anomalous subdomain.

Finally, the background subdomain fields are computed using inexpensive local substitutions. For each successive simulation, only the relatively small Schur complement system has to be solved, which results in significant computational savings. We applied this approach to two moderately sized 3D problems in marine controlled-source electromagnetic modeling: (1) a deepwater model in which the resistivities of the seawater and the air layer were kept fixed and (2) a model in which focused inversion was performed in a scenario in which the resistivities of the background formation, the air layer, and the seawater were known. We found a significant reduction of the modeling time in inversion that depended on the relative sizes of the constrained and unconstrained volumes: the smaller the unconstrained volume, the larger the savings. Specifically, for a focused inversion of the Troll oil field in the North Sea, the gain amounted up to 80% of the total modeling time.

INTRODUCTION

Having an efficient algorithm for 3D electromagnetic (EM) modeling is a key ingredient to survey design, inversion, and interpretation of controlled-source EM (CSEM) data in complex geologic settings. Several numerical approaches exist for 3D EM modeling in the frequency and time domains. Common approaches include the finite-difference (FD), finite-volume (FV), finite-element (FE), and integral equation (IE) methods; see, e.g., Avdeev (2005), Zhdanov (2009), and Börner (2010) for detailed reviews of these approaches. In the frequency domain, EM modeling reduces the governing partial differential equation (PDE) to one system of linear equations $\mathbf{Mx} = \mathbf{s}$ per frequency, where $\mathbf{M}$ is the system matrix defined by the medium properties and grid discretization, $\mathbf{x}$ is a vector of unknowns containing monochromatic EM fields, and $\mathbf{s}$ represents a monochromatic source and boundary conditions (Newman and

Alumbaugh, 1995). The FD and FE methods are the most popular methods; in both of these methods, the system matrix $\mathbf{M}$ is sparse and can be computed easily. This sparseness is crucial to make the solvers — direct, iterative, or hybrid — used to solve the system of linear equations fast and efficient.

During recent years, inversion has become the main tool to interpret CSEM data. Three-dimensional inversion converts the acquired CSEM signals over a given area to a 3D image of the subsurface resistivity distribution of that area. The presence or absence of hydrocarbons has been correctly predicted using CSEM inversion in numerous instances; for example, Fanavoll et al. (2012) and Gabrielsen et al. (2013) present CSEM inversion success stories in the Barents Sea covering many different geologic provinces including major recent discoveries: Skrugard, Havis, and Norvarg.

To recover a 3D, geologically consistent, resistivity image of subsurface, CSEM inversion algorithms usually require many forward

E315

simulations of CSEM responses over different resistivity models. Most of the time, these models differ from each other only within a smaller subdomain. In a marine environment, these situations occur for example in the following scenarios: (1) One knows the resistivities of the seawater and the air layer (Figure 1a) and allows the resistivities of the formation to be updated by inversion and (2) in addition to the seawater and the air layer resistivities, one also knows the resistivity of the background formation (Figure 1b) and allows the resistivity to be updated only within a smaller target reservoir. Scenario (1) is very common in marine CSEM surveys because the resistivity of the seawater is typically recorded during the survey and the resistivity of air is known. Scenario (2) may occur in the case of a producing field, e.g., the Frigg gas field (Hamilton et al., 2010), the Troll field (Gabrielsen et al., 2009), or the Snøhvit field (Gabrielsen et al., 2012), in which one has a good understanding of the background formation or in areas with existing seismic, well log, and/or magnetotelluric data giving confidence in the fine-scaled structures and resistivities of the background formation. Several CSEM surveys have been carried out over such areas to precisely locate hydrocarbon-bearing reservoirs by integrating CSEM results with seismic and well-log data, e.g., the above mentioned major recent discoveries presented by Fanavoll et al. (2012) and Gabrielsen et al. (2013) and the Bøyla discovery (Roth et al., 2013).

In such situations, the standard FD or FE methods would require rediscretizing the entire computational domain to simulate 3D CSEM responses for every new resistivity model even if the resistivities have changed only in a smaller subdomain. Alternatively, one can use the IE method, which permits running simulations only over the smaller anomalous subdomain after computing the dyadic Green's functions of the background/constrained subdomain (Zhdanov, 2009). This reduces the size of system matrix $\mathbf{M}$ dramatically. However, in the conventional IE method, the matrix $\mathbf{M}$ is dense, its computation is a tedious and nontrivial task involving evaluation of singular integrals, and sharp conductivity variations are difficult to handle (Zhdanov, 2009). These disadvantages of the IE method are quite serious, even though some progress has been reported on how to avoid computation of the whole dense matrix $\mathbf{M}$ (Avdeev and Knizhnik, 2009). Therefore, it might be more promising to look for hybrid approaches in which some of the above challenges are solved by invoking simpler FD/FE methods, whereas the main

computations are still restricted to the anomalous region only (Gupta et al., 1987). Recent progress here includes an extension of the IE method to an inhomogeneous background in which the background fields are computed using the FD method (Endo et al., 2010) and the IE method to compute a preconditioner for an iterative FD solver that effectively eliminates the background nodes from the iterative process (Zaslavsky et al., 2011).

In this paper, we present a new way to restrict simulations to the anomalous subdomain within the simple framework of the FD method via a Schur complement approach when using a direct solver. The underlying idea is to decompose the entire computational domain into two subdomains: a background subdomain and an anomalous subdomain. A sparse direct solver is used to remove the unknowns associated with the background subdomain and precompute the corresponding Schur complement in a first simulation. The Schur complement system is then solved to compute EM fields in the anomalous subdomain, followed by local backward substitutions that give EM fields in the background subdomain too. For subsequent simulations, one only has to solve the Schur complement system followed by local backward substitutions. Consequently, for each subsequent simulation, the large matrix factorization is reduced to the factorization of only a relatively small Schur complement matrix. This results in significant savings in modeling time, and hence, also in significantly reduced inversion times. The magnitude of the savings depends on the relative sizes of the background and anomalous volumes: the smaller the anomalous volume, the larger the savings. Moreover, the Schur complement approach is more efficient for inversion algorithms in which the forward modeling time contributes significantly to the inversion time.

The Schur complement is introduced by Haynsworth (1968) and has been widely used, for example, in an algebraic domain decomposition method in which the computational domain is divided into several smaller subdomains (Smith et al., 1996; Saad, 2003). A direct solver is used to remove subdomain interior unknowns by partially factorizing matrices assembled on each subdomain and computing the corresponding Schur complements. The Schur complement systems are then solved with an iterative solver to compute unknowns located at the interfaces among the subdomains. Finally, the subdomain interior unknowns are computed by local backward-forward substitutions. The approach is commonly referred to as a hybrid direct-iterative solver and has been applied to various geophysical problems (see, e.g., Lu and Shen, 1997; da Silva et al., 2010; Sourbier et al., 2011).

We use multifrontal massively parallel sparse direct solver (MUMPS) (Amestoy et al., 2001, 2006), a direct solver, to compute the Schur complement of the background subdomain by partial factorization of the matrix $\mathbf{M}$ and to solve the Schur complement system. MUMPS was developed based on the multifrontal approach (Duff et al., 1986; Liu, 1992) and parallelized using a hybrid model of parallelism. The application of direct solvers to 3D problems has \traditionally been considered to be computationally too demanding. However, recent advances in matrix-factorization algorithms, along with the availability of parallel computational resources, have created the necessary conditions to attract interest in factorization methods in the case of
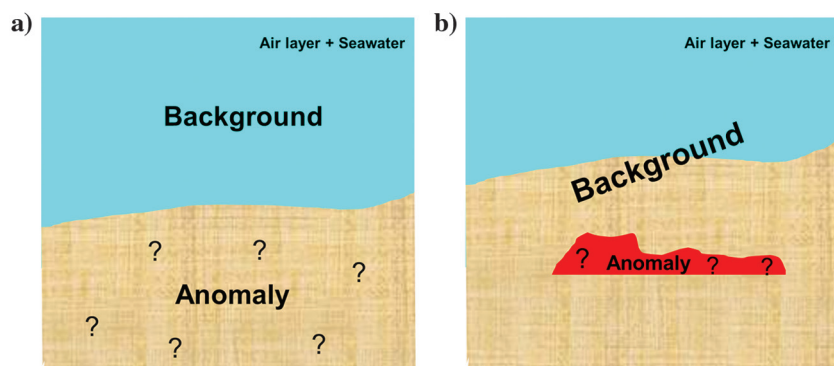

Figure 1. Sketches illustrating background and anomalous subdomains. Panel (a) illustrates a case in which the resistivities of the air layer and seawater are known, and panel (b) illustrates a case in which, in addition to the air layer and seawater resistivities, one also knows the background formation resistivity.

3D EM problems of moderate size, e.g., by Streich (2009), da Silva et al. (2012), Yang and Oldenburg (2012), Grayver et al. (2013), and Schwarzbach and Haber (2013).

In the remainder of this paper, we briefly describe the theory of frequency-domain FD (FDFD) followed by the theory and implementation of our Schur complement approach. We then validate our Schur complement scheme by comparing computed EM field values to corresponding values obtained using alternative, well-known modeling approaches. We thereafter illustrate the use of our Schur complement FDFD scheme on a deepwater CSEM example. The efficiency of this approach is subsequently discussed for a focused 3D inversion in which the background resistivities are constrained.

FINITE-DIFFERENCE ELECTROMAGNETIC SCHEME

If the temporal dependence of the EM fields is $e^{-i\omega t}$, then the corresponding frequency-domain Maxwell equations are

$$\nabla \times \mathbf{E} = i\omega\mu\mathbf{H} - \mathbf{K} \tag{1}$$

and

$$\nabla \times \mathbf{H} = (\sigma\mathbf{E} - i\omega\varepsilon\mathbf{E}) + \mathbf{J}, \tag{2}$$

where $\mathbf{E}$ and $\mathbf{H}$ are, respectively, the electric and magnetic fields, $\mathbf{J}$ and $\mathbf{K}$ are, respectively, electric and magnetic field sources, ω is angular frequency, and μ, ε, and σ are, respectively, the magnetic permeability, dielectric permittivity, and electrical conductivity of the medium.

By taking the curl of equation 1 and substituting equation 2, we obtain

$$\nabla \times \nabla \times \mathbf{E} - i\omega\mu(\sigma\mathbf{E} - i\omega\varepsilon\mathbf{E}) = i\omega\mu\mathbf{J} - \nabla \times \mathbf{K}. \tag{3}$$

Because in the CSEM method one typically uses low frequencies, in the range from 0.1 to 10 Hz, the displacement current can be neglected as $\sigma/(\omega\varepsilon) \gg 1$. Therefore, equation 3 is written as

$$\nabla \times \nabla \times \mathbf{E} - i\omega\mu\sigma\mathbf{E} = i\omega\mu\mathbf{J} - \nabla \times \mathbf{K}. \tag{4}$$

Equation 4 is a second-order PDE and forms the basis for CSEM modeling. To obtain a solution, this equation is discretized on a staggered Yee grid (Yee, 1966) following Newman and Alumbaugh (1995). The electric and magnetic field components are assigned to the edges and the faces of each cell, respectively (Figure 2). For a cell with the main node (i, j, k) located at the top left corner, the x, y, and z components of the electric field are located at $(i + \frac{1}{2}, j, k), (i, j + \frac{1}{2}, k)$, and $(i, j, k + \frac{1}{2})$, respectively. In the same cell, the x, y, and z components of the magnetic field are located at $(i, j + \frac{1}{2}, k + \frac{1}{2})$, $(i + \frac{1}{2}, j, k + \frac{1}{2})$, and $(i + \frac{1}{2}, j + \frac{1}{2}, k)$, respectively.

The resistivity within each cell is assumed to be constant. The above discretization requires resistivity values at each electric field node (halfway along a given cell edge). This is obtained by computing effective resistivity values at each node by properly averaging the resistivity of surrounding cells using an averaging method similar to that described in Davydycheva et al. (2003) or in Taflove and Hagness (2005, p. 492).

The FD discretization of equation 4 is assembled into a system of linear equations

$$\mathbf{Mx} = \mathbf{s}, \tag{5}$$

where $\mathbf{M}$ is the system matrix of dimension $(3N)^2$ for a modeling grid having $N = N_x \times N_y \times N_z$ cells, $\mathbf{x}$ is the unknown electric field vector of dimension $3N$, and $\mathbf{s}$ (dimension $3N$) is the source vector resulting from the right side of equation 4. The matrix $\mathbf{M}$ is a sparse complex matrix, having up to 13 nonzero elements in a row if one uses second-order finite differences. The off-diagonal entries of $\mathbf{M}$ are real and depend only on the grid spacing while the diagonal entries are complex and depend on the grid spacing as well as the medium conductivity, the magnetic permeability, and the frequency. In our modeling, the variations in the magnetic permeability are not considered, and it is assumed that $\mu = \mu_0 = 4\pi \times 10^{-7}$ H/m.

Air layer and boundary conditions

A highly resistive thick air layer above the seawater is also included in the model. This air layer is discretized with severely stretched nonuniform cells whose thicknesses in the z-direction grow as we move up from the sea surface as $dz(n) = dz(0) \times \lambda^n$, where $n = 0, 1, 2, \ldots, dz(0)$ is z-dimension of the top cell in the sea and λ is a constant. During tests for various 1D models against quasi-analytical solutions (Løseth and Ursin, 2007), it was observed that an air layer of resistivity $\sim 10^7$ Ωm and thickness ~ 70 km, discretized with ~ 15 severely stretched nonuniform cells, provides good accuracy (see the "Examples" section). The last two parameters and $dz(0)$ define the constant λ, e.g., for $dz(0) = 100$ m, we get $\lambda \approx 1.43$.

Toward the static limit ($\omega \to 0$) in the highly resistive air layer, the second term in equation 4 becomes negligible leading to nonuniqueness of solution. Accordingly, it is common to enforce a static divergence correction $\nabla \cdot \sigma\mathbf{E} = 0$. This correction, originally introduced to improve the convergence of iterative solvers (Smith, 1996) is sometimes also used at very low frequencies with direct solvers (Grayver et al., 2013). However, for typical CSEM
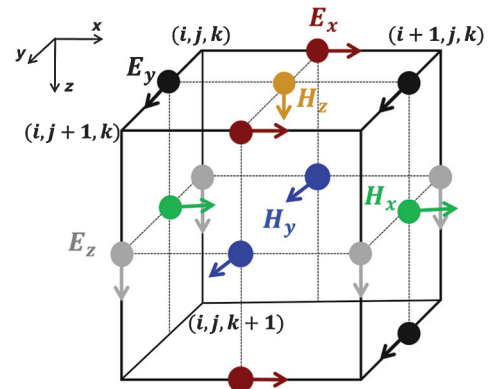

Figure 2. The staggered Yee grid used to define the positions of the electric and magnetic field nodes. The electric field components are assigned to cell edges and the magnetic field components to cell faces.

frequencies ($\sim 0.1 - 10$ Hz) our experience is that this is not necessary for direct solvers, which is in agreement with, e.g., Streich (2009) and da Silva et al. (2012).

At all sides of the computational domain, Dirichlet boundary conditions are applied by setting the electric field values to zero. Moreover, we add seven nonuniform cells at the lateral and bottom boundaries of the computational domain. Stretching for these cells is done using the power law discussed above for the air layer with $\lambda = 2$. These stretched cells significantly reduce inaccuracies related to the finite extent of the computational domain.

SCHUR COMPLEMENT APPROACH

In this section, we describe our Schur complement-based FDFD modeling approach. We assume that the forward modeling will be used in constrained CSEM inversion schemes in which only certain parts of the earth model can change their physical properties.

Matrix equations

Let us divide the computational domain into two subdomains a and b. The background subdomain b consists of the unknowns associated with the part of the model in which resistivities are kept fixed, whereas the anomalous subdomain a consists of the unknowns associated with the part of the model in which resistivities are allowed to vary in the multimodel simulations. The linear system in equation 5 written in block form for this decomposition of the computational domain reads,

$$\begin{bmatrix} \mathbf{M}_{bb} & \mathbf{M}_{ba} \\ \mathbf{M}_{ab} & \mathbf{M}_{aa} \end{bmatrix} \begin{bmatrix} \mathbf{x}_b \\ \mathbf{x}_a \end{bmatrix} = \begin{bmatrix} \mathbf{s}_b \\ \mathbf{s}_a \end{bmatrix}, \qquad (6)$$

where $\mathbf{M}_{bb}$ is a block matrix having coefficients involving only unknowns in subdomain b, whereas matrix $\mathbf{M}_{aa}$ involves unknowns in subdomain a. Matrix $\mathbf{M}_{ba}$ represents the influence of the unknowns in subdomain b on the unknowns in subdomain a. Similarly, $\mathbf{M}_{ab}$ represents the influence of the unknowns in subdomain a on the unknowns in subdomain b. The off-diagonal matrices $\mathbf{M}_{ba}$ and $\mathbf{M}_{ab}$ are independent of the physical properties of the medium and only depend on the grid spacings.

A block LU factorization of $\mathbf{M}$ into two-by-two block matrices gives

$$\mathbf{M} = \begin{bmatrix} \mathbf{M}_{bb} & \mathbf{M}_{ba} \\ \mathbf{M}_{ab} & \mathbf{M}_{aa} \end{bmatrix} = \begin{bmatrix} \mathbf{L}_{bb} & 0 \\ \mathbf{L}_{ab} & \mathbf{L}_{aa} \end{bmatrix} \begin{bmatrix} \mathbf{U}_{bb} & \mathbf{U}_{ba} \\ 0 & \mathbf{U}_{aa} \end{bmatrix} = \mathbf{L}\mathbf{U}, \qquad (7)$$

where $\mathbf{L}_{bb}, \mathbf{L}_{ab}$, and $\mathbf{L}_{aa}$ are the blocks of block lower triangular matrix $\mathbf{L}$, and $\mathbf{U}_{bb}$, $\mathbf{U}_{ba}$, and $\mathbf{U}_{aa}$ are the blocks of block upper triangular matrix $\mathbf{U}$. The blocks $\mathbf{L}_{bb}$ and $\mathbf{U}_{bb}$ are lower and upper triangular matrices, respectively, which can be computed via an LU factorization of $\mathbf{M}_{bb}$ (i.e., $\mathbf{M}_{bb} = \mathbf{L}_{bb}\mathbf{U}_{bb}$). The blocks $\mathbf{L}_{ab}$ and $\mathbf{U}_{ba}$ are such that $\mathbf{L}_{ab}\mathbf{U}_{bb} = \mathbf{M}_{ab}$ and $\mathbf{L}_{bb}\mathbf{U}_{ba} = \mathbf{M}_{ba}$. Finally,

$$\mathbf{S} = \mathbf{L}_{aa}\mathbf{U}_{aa} = \mathbf{M}_{aa} - \mathbf{L}_{ab}\mathbf{U}_{ba} = \mathbf{M}_{aa} - \mathbf{M}_{ab}\mathbf{M}_{bb}^{-1}\mathbf{M}_{ba} \quad (8)$$

is the Schur complement matrix, where $-\mathbf{M}_{ab}\mathbf{M}_{bb}^{-1}\mathbf{M}_{ba}$ represents the contribution from the factorized background subdomain b to the unfactorized anomalous subdomain a (Zhang, 2005).

Equation 6 can be rewritten using equations 7 and 8:

$$\begin{bmatrix} \mathbf{M}_{bb} & \mathbf{M}_{ba} \\ \mathbf{M}_{ab} & \mathbf{M}_{aa} \end{bmatrix} \begin{bmatrix} \mathbf{x}_b \\ \mathbf{x}_a \end{bmatrix} = \begin{bmatrix} \mathbf{L}_{bb} & 0 \\ \mathbf{L}_{ab} & \mathbf{I} \end{bmatrix} \begin{bmatrix} \mathbf{U}_{bb} & \mathbf{U}_{ba} \\ 0 & \mathbf{S} \end{bmatrix} \begin{bmatrix} \mathbf{x}_b \\ \mathbf{x}_a \end{bmatrix}$$
$$= \begin{bmatrix} \mathbf{s}_b \\ \mathbf{s}_a \end{bmatrix}. \qquad (9)$$

Once the partial factorization has been performed, one can compute an intermediate vector $\mathbf{y}$ by forward substitution using

$$\begin{bmatrix} \mathbf{L}_{bb} & 0 \\ \mathbf{L}_{ab} & \mathbf{I} \end{bmatrix} \begin{bmatrix} \mathbf{y}_b \\ \mathbf{y}_a \end{bmatrix} = \begin{bmatrix} \mathbf{s}_b \\ \mathbf{s}_a \end{bmatrix}. \qquad (10)$$

To proceed further we notice that

$$\begin{bmatrix} \mathbf{U}_{bb} & \mathbf{U}_{ba} \\ 0 & \mathbf{S} \end{bmatrix} \begin{bmatrix} \mathbf{x}_b \\ \mathbf{x}_a \end{bmatrix} = \begin{bmatrix} \mathbf{y}_b \\ \mathbf{y}_a \end{bmatrix}, \qquad (11)$$

which simply reduces to

$$\mathbf{S}\mathbf{x}_a = \mathbf{y}_a \qquad (12)$$

and

$$\mathbf{U}_{bb}\mathbf{x}_b = \mathbf{y}_b - \mathbf{U}_{ba}\mathbf{x}_a. \qquad (13)$$

To compute the unknowns $\mathbf{x}_a$ in subdomain a, one needs to solve the Schur complement matrix equation 12. Finally, backward substitution can be applied to compute the unknowns $\mathbf{x}_b$ in subdomain b using equation 13.

Let us now consider a new medium in which the physical properties of subdomain a have changed, whereas those of the background subdomain b remain the same. It follows that $\mathbf{M}_{bb}$, and hence the matrices $\mathbf{L}_{bb}$ and $\mathbf{U}_{bb}$ representing its factorized form, also remain the same. As mentioned above, the off-diagonal matrices $\mathbf{M}_{ba}$ and $\mathbf{M}_{ab}$ do not depend on the medium resistivities, hence the matrices $\mathbf{L}_{ab}$ and $\mathbf{U}_{ba}$ also remain same. It then follows from equation 10 that the intermediate vector $\mathbf{y}$ will also remain unchanged. Hence, to find the unknowns $\mathbf{x}'$ for the modified medium using equation 11, one only lacks the modified Schur complement $\mathbf{S}' = \mathbf{M}'_{aa} - \mathbf{M}_{ab}\mathbf{M}_{bb}^{-1}\mathbf{M}_{ba}$, where matrix $\mathbf{M}'_{aa}$ is assembled on the anomalous subdomain of the new model. Recalling again the nondependency of the off-diagonal matrices $\mathbf{M}_{ba}$ and $\mathbf{M}_{ab}$ on the medium resistivities, the whole term $\mathbf{M}_{ab}\mathbf{M}_{bb}^{-1}\mathbf{M}_{ba}$ remains unchanged as long as the physical properties of the background subdomain b are unchanged. Thus, the new Schur complement matrix $\mathbf{S}'$ can be trivially obtained from the original Schur complement matrix $\mathbf{S}$ as

$$\mathbf{S}' = \mathbf{S} - \mathbf{M}_{aa} + \mathbf{M}'_{aa}. \qquad (14)$$

One thus needs to carry out the following three steps to find the unknowns for a medium with modified resistivities in the anomalous subdomain: (1) compute the modified Schur complement using equation 14, (2) get unknowns $\mathbf{x}'_a$ in subdomain a by solving the modified Schur complemented system $\mathbf{S}'\mathbf{x}'_a = \mathbf{y}_a$, and (3) compute the unknowns $\mathbf{x}'_b$ in subdomain b by backward substitution using equation 13. Importantly, one does not have to solve equation 5 for the whole system again. One has to solve only equation 12 for the unknowns $\mathbf{x}'_a$ in the anomalous subdomain followed by backward

substitutions for the unknowns $\mathbf{x}'_b$ in the background subdomain. It will take much less time provided that the anomalous subdomain is considerably smaller than the whole system.

Practical implementation

Figure 3 shows a 2D slice of the staggered Yee grid used for FD 3D simulations. The dots indicate locations of the grid nodes; the given slice in the x-z plane contains only E_x and E_z nodes. As previously explained, the computational domain is divided into two subdomains: a background subdomain b (shaded white) and an anomalous subdomain a (shaded blue). In multimodel simulations, the resistivities are allowed to change only in the anomalous subdomain, whereas in the background subdomain they must stay the same. In the following paragraph, we explain which nodes of the Yee grid become anomalous nodes corresponding to the unknowns $\mathbf{x}_a$ and which nodes of the Yee grid become background nodes corresponding to the unknowns $\mathbf{x}_b$.

In our FD scheme, each node is assigned a resistivity value obtained by averaging the resistivity over a volume surrounding the node. Hence, resistivities assigned at the nodes lying at the interface between the background and anomalous subdomains are also affected by the anomalous subdomain resistivities. For example, E_x and E_z nodes lying at the interface between the background and anomalous subdomains (depicted with red lines in Figure 3) are affected by the resistivities of the anomalous subdomain cells. A similar argument is also valid for E_y nodes lying at the interface between the background and anomalous subdomains. On the other hand, the resistivities of the nodes lying in the background subdomain only half a cell away from the interface between the background and anomalous subdomains do not depend on the resistivities of the anomalous subdomain. We shall define the anomalous nodes as the nodes whose resistivities depend on the anomalous subdomain resistivities and the background nodes as the nodes whose resistivities are independent of the anomalous subdomain resistivities. Consequently, the anomalous nodes include (1) all interior nodes in the anomalous subdomain, and (2) all nodes lying at the interface between the background and anomalous subdomains. The remaining nodes in the background subdomain are the background nodes.

Figure 4a shows the pattern of the system matrix $\mathbf{M}$ that is obtained by discretizing the governing PDE (equation 4) on a Yee grid, whereas Figure 4b shows the pattern of the Schur complement matrix $\mathbf{S}$ obtained by eliminating the background unknowns $\mathbf{x}_b$ from matrix equation 9. It can be seen that the Schur matrix $\mathbf{S}$ contains a small dense block. This is because matrix $\mathbf{M}_{bb}^{-1}$ in general is dense while matrices $\mathbf{M}_{ab}$ and $\mathbf{M}_{ba}$ are sparse with nonzero coefficients only for the unknowns in the vicinity of the interface between the background and anomalous subdomains. Therefore, the product $-\mathbf{M}_{ab}\mathbf{M}_{bb}^{-1}\mathbf{M}_{ba}$ is sparse with a small dense block corresponding to certain unknowns. These unknowns actually represent the nodes lying at the interface between the background and the anomalous subdomains. We call this interface the Schur interface. The Schur complement of the background unknowns only affects the nodes lying at the Schur inter-

face; this is why the rest of the matrix $\mathbf{S}$ remains intact and very sparse. Furthermore, every node at the Schur interface becomes connected to all other nodes there, through the eliminated background nodes, which results in a very dense block, essentially
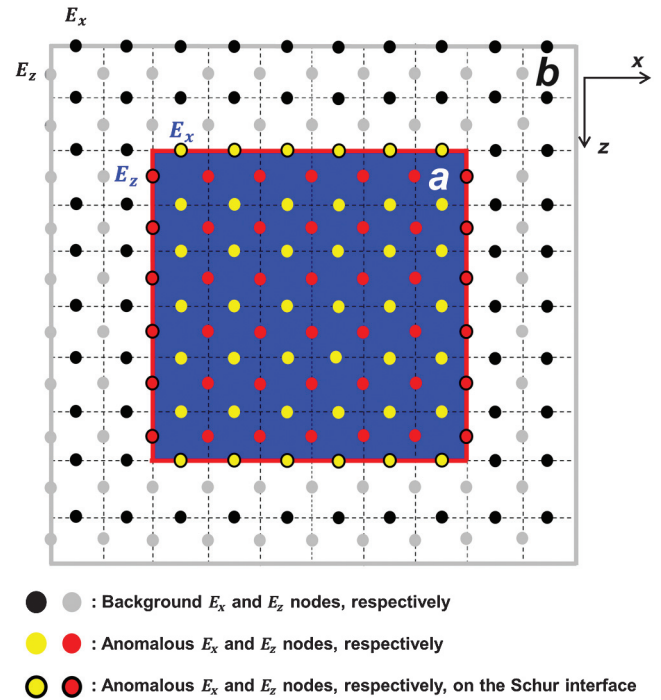

Figure 3. Sketch of a 2D slice of the staggered Yee grid used for FD 3D simulations. The dots indicate the location of the grid nodes; this slice in the x-z plane contains only E_x and E_z nodes. The red line, separating the anomalous subdomain a from the background subdomain b, is the Schur interface. The yellow and red color nodes lying on the Schur interface and the interior of the anomalous subdomain are anomalous nodes and correspond to the unknowns $\mathbf{x}_a$. The remaining nodes lying outside of the Schur interface are background nodes and correspond to the unknowns $\mathbf{x}_b$.
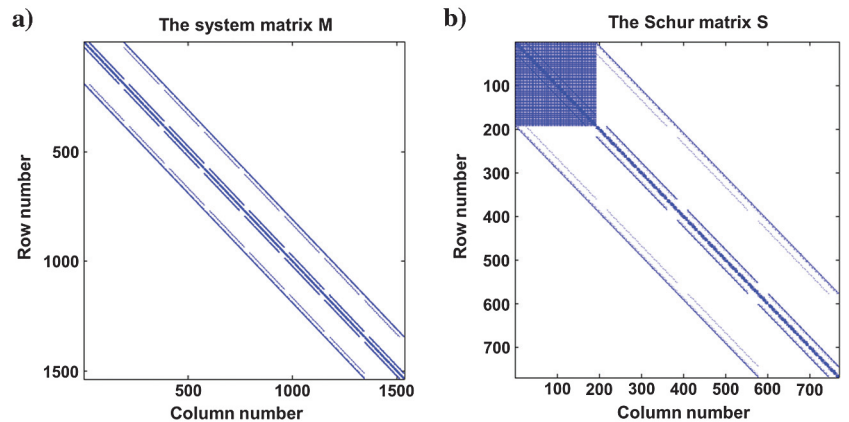

Figure 4. (a) The pattern of system matrix $\mathbf{M}$ in equation 5 discretized on an $8 \times 8 \times 8$ grid and (b) the Schur complement matrix $\mathbf{S}$ in equation 12 obtained by removing the background unknowns $\mathbf{x}_b$ from equation 9. The matrix $\mathbf{S}$ is dense for the unknowns lying on the Schur interface and remains sparse and the same as the matrix $\mathbf{M}_{aa}$ for the interior anomalous subdomain unknowns (Figure 3). For realistic CSEM problems with millions of unknowns, the dense part of $\mathbf{S}$ occupies in the order of $1\% \times 1\%$ of the matrix $\mathbf{S}$.

without nonzero elements. A similar pattern for Schur complement matrices can be seen in domain decomposition approaches; see, for example, Smith et al. (1996) and Saad (2003).

This property of the Schur complement matrix **S** allows us to compute it efficiently. Namely, we may consider only the background unknowns, the unknowns lying at the Schur interface, and the unknowns within two layers of anomalous subdomain cells away from the Schur interface to compute the dense diagonal block of **S**. This block constitutes part of the term $-\mathbf{M}_{ab}\mathbf{M}_{bb}^{-1}\mathbf{M}_{ba}$ in equation 8. After that we build the total Schur complement matrix **S** by adding the matrix $\mathbf{M}_{aa}$ for the interior anomalous subdomain unknowns. Separate handling of the dense block of $-\mathbf{M}_{ab}\mathbf{M}_{bb}^{-1}\mathbf{M}_{ba}$ and the sparse $\mathbf{M}_{aa}$ allows a much more efficient usage of computer memory.

Another practical recommendation is related to the use of equation 14 when resistivities in the anomalous subdomain have been updated (e.g., by a constrained CSEM inversion algorithm) and one needs to compute the updated Schur complement matrix $\mathbf{S}'$. The operations in equation 14 can be performed only on the diagonal elements because the off-diagonal entries of $\mathbf{M}_{aa}$ and $\mathbf{M}'_{aa}$ are identical; they do not depend on the resistivities, but only on the grid spacings, as mentioned earlier.

A direct sparse solver, MUMPS (Amestoy et al., 2001, 2006), was used to compute the Schur complement of the background unknowns $\mathbf{x}_b$ by partial factorization of the matrix **M**. MUMPS, being a multifrontal solver, has the nice property that partial factorization of $\mathbf{M}_{bb}$ naturally provides its Schur complement to the anomalous subdomain without actually performing operations in equation 8. The Schur complement is commonly referred to as "contribution block" in the multifrontal solver nomenclatures (Amestoy et al., 2001). Being mostly a sparse system of equations, the Schur complement system $\mathbf{S}\mathbf{x}_a = \mathbf{y}_a$ is also solved with MUMPS.

EXAMPLES

In this section, we validate the accuracy of the developed modeling algorithms against well-established methods. We then illustrate the efficiency of our Schur complement-based FDFD approach with two cases: a deepwater inversion with constrained seawater and air layer, and a focused inversion in which resistivity is only updated within a reservoir volume.

Validation against a layered earth model response

Let us examine the performance of our FDFD algorithms using the layered earth model from Figure 5. The dimension of the model is $20 \times 20 \times 5$ km^3. The FD grid has a spacing of 100 m in the x-direction and 200 m in the y-direction. In the z-direction, the spacing is nonuniform, with minimum and maximum spacings of, respectively, 30 and 200 m. Except for the top side, each side of the model is padded with seven nonuniform cells to accommodate boundary conditions. The top side includes an air layer of thickness ~70 km and resistivity 10^7 Ωm. The discretization of these additional layers (not shown in Figure 5) was discussed above. The discretization of the FD grid model results in $214 \times 114 \times 79$ cells, representing approximately 5.78×10^6 degrees of freedom. The transmitter is an x-oriented horizontal electric dipole with a frequency of 0.25 Hz and located 30 m above the seabed.

The solution of the resulting linear system was computed using eight nodes, each having sixteen cores and 128 GB of memory. The

total simulation time was 18,171 s. The memory allocated at each processor was of approximately 4.4 GB. The 3D simulation results, obtained through the FDFD method, are compared with reference fields calculated using a semianalytical plane-layer method (Løseth and Ursin, 2007). The air conductivity is set to zero in the semianalytical calculations. Figure 6 shows the amplitude and phase responses for the x and z components of the electric fields along a receiver line placed at the seabed. The solid lines and filled circles, respectively, show results obtained with the FDFD and semianalytical methods. Except for the responses that are close to the transmitter position, the field amplitudes differ at most by 1.0% and the phases by at most by 0.8°. Note that the responses obtained with and without the use of a Schur complement approach are identical; we do not lose accuracy using Schur complement-based FDFD approach.

The examples below illustrate the efficiency of our Schur complement-based FDFD approach, but they also serve as validation of our FDFD code for 3D models against fast FD time-domain (FDTD) modeling code (Maaø, 2007; Mittet, 2010). Frequency-domain fields are computed from the FDTD code using Fourier transforms and then plotted together with results of FDFD code.

Deepwater controlled-source electromagnetic inversion: Gulf of Mexico

In a marine environment, the depth profile of seawater conductivity is routinely measured using a conductivity-temperature-depth (CTD) profiler during the acquisition of CSEM data. The CTD measurements are usually done at different locations of the CSEM survey to learn how the seawater conductivity profile varies laterally. As a result, the seawater conductivity distribution is known rather accurately, and its variations in all three directions can be traced. Therefore, it is common practice not to invert for the seawater resistivities, in particular because inversion is usually faster with a small number of unknowns. In addition, the resistivity of the air layer is usually fixed to a sufficiently high value (in our case 10^7 Ωm), and small variations in it have almost no effect on the computed EM fields. Therefore, it does not make any sense to invert for the air layer resistivity either.

In deepwater environments, the thick air and seawater layer may represent nearly half of the total computational domain. The number of floating point operations required for factorization scales with the matrix size as $\mathcal{O}(N^2)$. Because inversion requires many forward simulations for different resistivity models, precomputing contributions from air and seawater in the form of a Schur complement can lead to saving more than half of the time spent on forward modeling.

Let us consider a realistic deepwater model based on a case of the Perdido fold belt with northeast–southwest-trending anticlines in deepwater $(2.5-3.2$ km$)$ of the northwestern Gulf of Mexico. A marine CSEM survey was carried out in 2008 with a base frequency of 0.2 Hz, covering about 1000 km^2 of the Alaminos Canyon and targeting some petroleum prospects in the area. Part of the area was later reacquired with higher frequencies (0.5, 1.5, 2.0, and 2.5 Hz) to image more accurately the Wilcox discovery beneath shallow gas hydrate (Kanhalangsy et al., 2011). Here, a total of 75 seabed receivers were used to acquire CSEM data with a dense inline receiver spacing of 0.5 and 1 km, respectively, near and far from the area of interest and interline spacing of 4 km.

The anisotropic 3D CSEM inversion is based on a quasi-Newton update and is described by Zach et al. (2008). First, we perform direct modeling in the reciprocal mode meaning that the receivers become the computational transmitters and then adjoint modeling to compute the gradients. At each iteration, this inversion requires about 600 modeling jobs (four field components [$\mathbf{E}_x$, $\mathbf{E}_y$, $\mathbf{H}_x$, and $\mathbf{H}_y$] $\times$ 2 [direct and adjoint modeling] $\times$ number of receivers) with different transmitters for the same resistivity model. With a direct solver, once the matrix is factorized, responses for all transmitters are obtained using local backward-forward substitutions. The time spent for backward-forward substitutions is nearly the same with and without the use of a Schur complement approach.

Start models for CSEM inversion of the reacquired data based on the geologic horizons are shown in Figure 7 for horizontal and vertical resistivity. The seawater resistivities vary in the range 0.2−0.3 Ωm, and the background horizontal and vertical resistivities vary in the ranges 1.0−2.0 Ωm and 1.5−2.5 Ωm, respectively. The dimension of the FD grid model is $20 \times 18 \times 6.5$ km^3 and was discretized with grid spacings of 400 m in the x- and y-directions and 50 m in the z-direction. The resistivity models include an air layer above the seawater and are padded with seven nonuniform cells at the remaining five sides as in the layered earth model example (these additional layers are not shown in Figure 7). The discretization of the FD grid model results in $65 \times 60 \times 153$ cells, representing approximately 1.79×10^6 degrees of freedom. The transmitter is an x-oriented horizontal electric dipole placed 30 m above the seabed and has a base frequency of 0.5 Hz.

The simulations using standard FDFD and Schur complement-based FDFD approaches were performed using four computational nodes, each having 16 cores and 128 GB of memory. The Schur interface was defined in the x-y-plane at 2.5 km below the sea surface (the white dashed line in Figure 7) for the Schur complement-based FDFD approach. This results in $65 \times 60 \times 66$ cells in the background and $65 \times 60 \times 87$ cells in the anomalous subdomains. All unknowns above the Schur interface are eliminated, and their contributions at the Schur interface are obtained via the Schur complement. Higher frequencies 1.5, 2.0, and 2.5 Hz were also used in simulations on the same grid to see the performance of our approach for different system matrices $\mathbf{M}$ (even though for accurate inversions at higher frequencies, one would normally need a finer grid). Figure 8 shows the amplitude and phase response curves for the x component of the electric field along a receiver line at $y = 0$ placed on the seabed. The solid lines represent the 3D FDFD method, and the filled circles represent the 3D FDTD method. The relative error among these two approaches always stays within 1.0%.

Anisotropic 3D CSEM inversion for this data set required approximately 140 iterations over earth models with different background and target resistivities to converge to a good final model (C. Kanhalangsy, personal communication, 2013). Table 1 shows the memory and run time for the modeling jobs run by inversion

using FDFD with and without the Schur complement approach. Numbers in Table 1 are for one frequency only, whereas numbers for other frequencies follow a very similar trend (as expected for a direct solver). Furthermore, note that the number of unknowns when computing the Schur complement is less than the total number of unknowns in the model; this is because we consider only those nodes that are in the background subdomain, Schur interface, and two layers of anomalous cells below the Schur interface when computing the Schur complement of the background subdomain.

For each frequency, the standard FDFD method took 3548 s to factorize the system matrix $\mathbf{M}$ and 1297 s for the backward-forward substitutions to compute the responses for all 600 computational transmitters, whereas the Schur complement approach took 1747 s to compute the Schur complement $\mathbf{S}$ by partial factorization of $\mathbf{M}$,
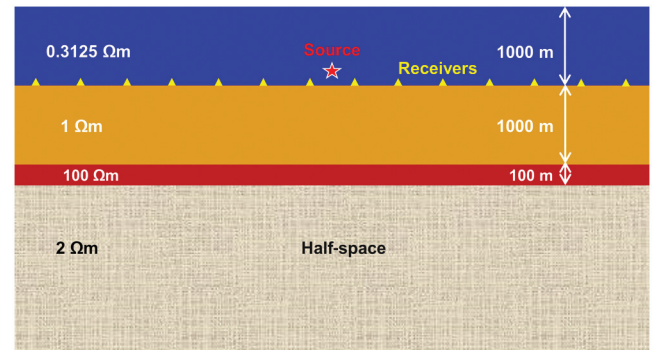

Figure 5. Vertical cross section through the layered earth model used for comparison with plane-layer solutions.
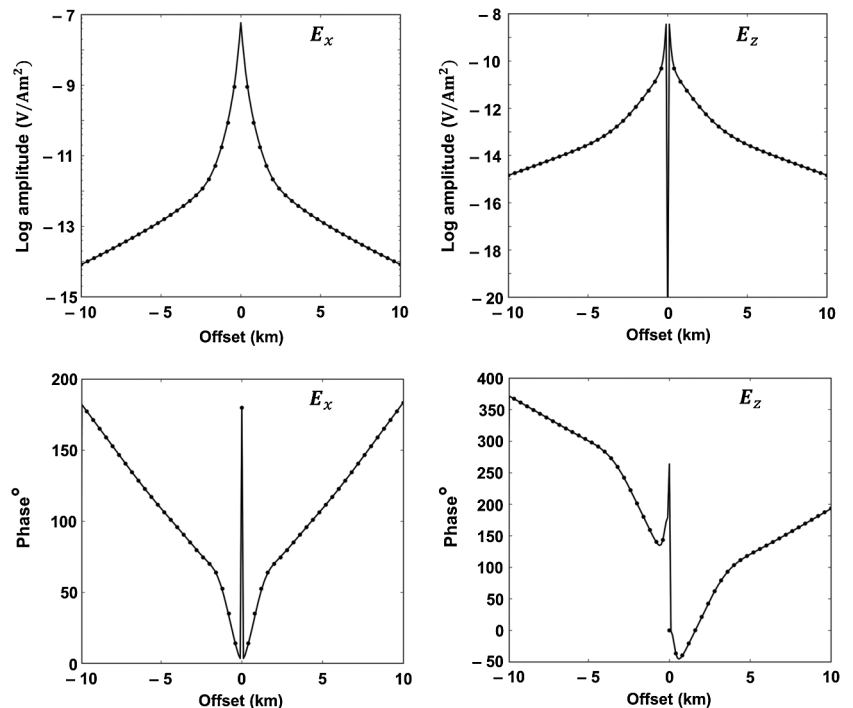

Figure 6. Comparison of electric field responses at 0.25 Hz for the layered earth model in Figure 5 calculated using our FDFD approach (solid lines) and the plane-layer modeling of Løseth and Ursin (2007) (filled circles). The field responses are plotted along a receiver line placed at the seabed.

203 s to compute intermediate vector $\mathbf{y}$ using forward substitutions, 2070 s to factorize $\mathbf{S}$, 584 s to compute anomalous subdomain fields $\mathbf{x}_a$ using substitutions, and 509 s to compute background subdomain fields $\mathbf{x}_b$ using backward substitutions. For the first iteration, modeling jobs take $1747 + 203 + 2070 + 584 + 509 = 5113$ s using the Schur complement-based FDFD approach, making it slower than the standard FDFD approach that takes $3548 + 1297 = 4845$ s. However, for multimodel simulations, the situation is different because the Schur complement and intermediate vector only need to be computed once. Every subsequent run of the Schur complement-based FDFD approach needs only the time to factorize $\mathbf{S}$ and the time to compute $\mathbf{x}_a$ and $\mathbf{x}_b$ using substitutions, i.e., $2070 + 584 + 509 = 3163$ s to simulate CSEM responses for the entire model with all computational transmitters. Therefore, the total modeling time for the entire CSEM inversion requiring 140 iterations would then be $(1747 + 203 + 140 \times 3163)\,\text{s} = 444{,}770\,\text{s} \approx 5.1\,\text{days}$ with the Schur complement approach as compared with $140 \times 4845\,\text{s} = 678{,}300\,\text{s} \approx 7.9\,\text{days}$ with standard FDFD modeling.

We have analyzed how the total modeling times scale with the number of iterations and transmitters (see Figure 9). Figure 9a shows a plot of modeling times as a function of the number of iterations for a constant number of transmitters (600), whereas Figure 9b shows a plot of modeling times as a function of the number of transmitters for a constant number of iterations (140). From these plots, we observe that for a realistic CSEM inversion — assuming around 100 iterations with a few hundred transmitters

— one can save up to about 35%–40% of the total modeling times using the Schur complement-based FDFD approach.

Focused inversion: Troll oil field

The Troll field, which is the biggest gas field in the North Sea, also has oil in a thin zone under the gas trap. The field extends over three fault blocks tilted east and is subdivided into Troll East, the Troll West Gas Province, and the Troll West Oil Province (TWOP) (Mikkelsen et al., 2005). The TWOP is a smaller (25 km^2) segment of the reservoir in which the oil column has a thickness of 15–27 m. A 3D marine CSEM survey over the Troll oil field was acquired in 2008 as part of R&D collaboration between Statoil and Electromagnetic Geoservices (EMGS) (Gabrielsen et al., 2009).

For this producing field, abundant information about the background formation is available from seismic and well-log data. One can use the background formation resistivities obtained from
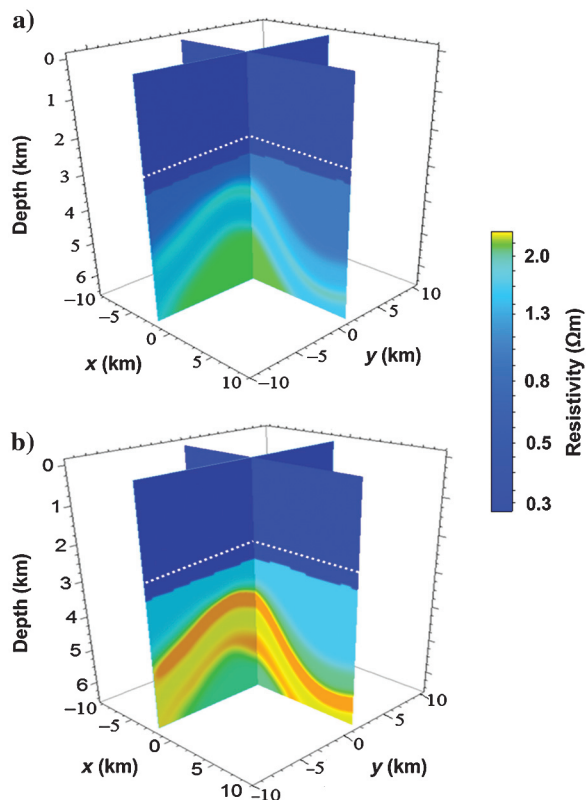

Figure 7. (a) Horizontal and (b) vertical resistivity models from the deepwater Gulf of Mexico used for synthetic simulations of CSEM responses. The white dashed line shows the Schur interface placed in the x-y-plane at a depth of 2.5 km below the sea surface.
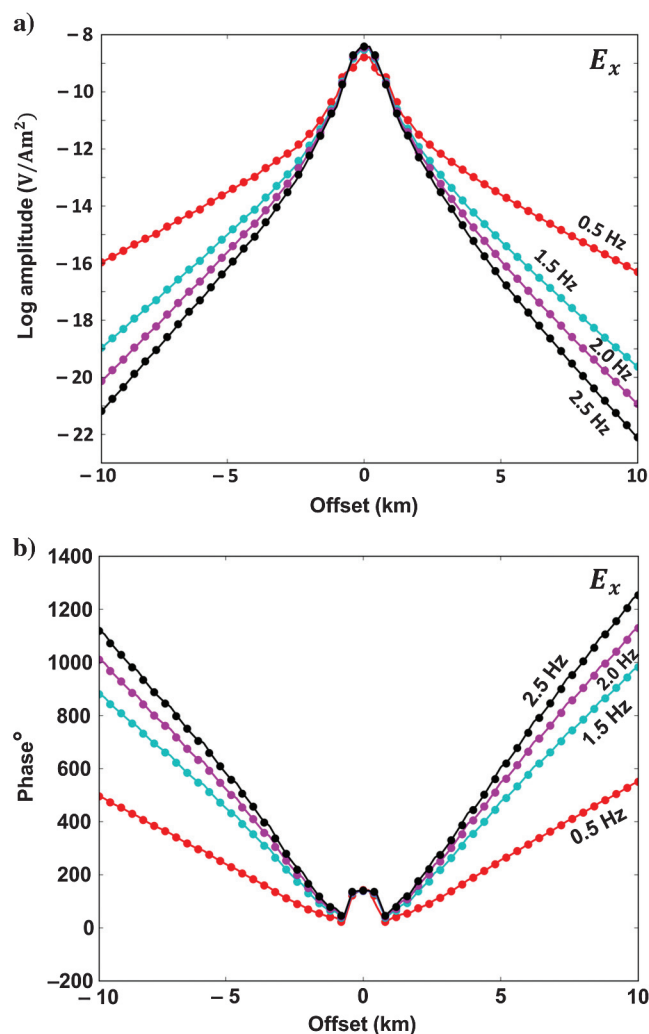

Figure 8. The (a) amplitude and (b) phase responses of the x-component of the electric field for the deepwater model from the Gulf of Mexico (Figure 7) calculated using FDFD (solid lines) and FDTD (filled circles) for the frequencies 0.5, 1.5, 2.0, and 2.5 Hz. The field responses are plotted along a receiver line $y = 0$ km placed on the seabed.

the well-log data interpretations and the fine-scaled structural information obtained from the seismic data interpretations. A focused CSEM inversion, in which only the target reservoir resistivities are allowed to change while other resistivities are kept constant, can then be a good choice. In the following paragraphs, we will compare the modeling time required for running such an inversion using FDFD modeling with and without the Schur complement approach.

We took the same resistivity model used by Morten et al. (2012) in which CSEM data from 54 seabed receivers were inverted to obtain the distribution of hydrocarbon saturation in the TWOP reservoir. Figure 10 shows the 3D cubes of horizontal and vertical resistivities obtained at intermediate steps of this anisotropic 3D CSEM inversion. The resistivity of the seawater is 0.27 Ωm; the background horizontal resistivities vary from 1.5 Ωm in the shallow part to $2.1-2.3 \times$ Ωm below 2000 m depth. The background vertical resistivities vary in the range $2.1-4.5$ Ωm. The horizontal and vertical resistivities within the target reservoir vary in the ranges $23.0-30.0$ Ωm and $65.0-80.0$ Ωm, respectively. The FD grid model has a dimension of $20 \times 12 \times 3.5$ km^3 and was discretized with grid spacings of 200 m in the x- and y-directions and 30 m in the z-direction. The resistivity models include an air layer and are padded with seven nonuniform cells as in the case of the layered earth model example. The discretization of the FD grid model results in $115 \times 75 \times 140$ cells, representing approximately 3.62×10^6 degrees of freedom. The transmitter is an x-oriented horizontal electric dipole placed 30 m above the seabed; the operating frequencies of the transmitter are 0.25, 0.75, and 1.25 Hz. Figure 11 shows the amplitude and phase responses of the x-component of the electric field along a receiver line at $y = 3$ km on the seabed. The solid lines are for the FDFD method and the filled circles for the FDTD method. The relative error among the two stays within 1.5%.

The computational resources used for the standard FDFD simulations and the Schur complement-based FDFD simulations were the same as those for the layered earth model example. For simulations based on the Schur complement approach, we defined the Schur interface on the boundary of an approximately $8 \times 5 \times 0.3$ km^3 volume
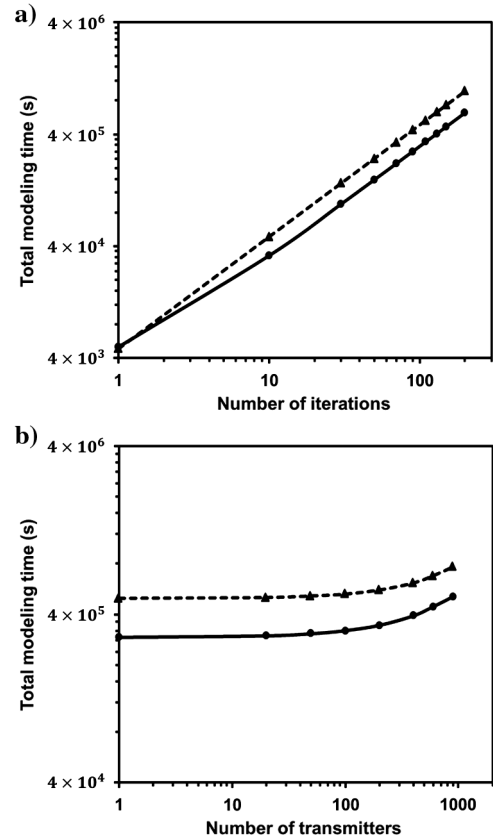

Figure 9. (a) Plots showing the influence of the number of iterations and (b) the number of transmitters on the total modeling times for a CSEM inversion. The Schur complement-based FDFD (solid line) provides a significant reduction of the total modeling time as compared with standard FDFD (dashed line) unless the number of iterations is too small or number of transmitters is too large. The plots were generated for the deepwater model from the Gulf of Mexico.

Table 1. Memory requirements and observed run time per frequency for performing CSEM modeling with and without the Schur complement approach for the deepwater model from the Gulf of Mexico in Figure 7. CSEM modeling is performed for 600 computational transmitters. Here N is the number of unknowns, NNZ the number of nonzero coefficients, M_f (GB) the total amount of memory used during factorization, M_p (GB) the peak memory at one of processors needed to store matrix S, T_f (s) the factorization time, and T_s (s) the backward or forward substitution time for 600 right-hand sides (RHSs). The column labeled T (days) shows the projected total modeling time per frequency for a CSEM inversion requiring 140 iterations. Use of the Schur complement-based approach reduces this time by approximately 35%.

		Standard FDFD modeling				
N	NNZ	M_f (GB)	M_p (GB)	T_f (s)	T_s (s)	T (days)
1,790,100	22,995,556	143	3	3548	1297	~7.9

Compute **S** by partial factorization of **M**						Compute **y**	Compute $\mathbf{x}_a$ by solving $\mathbf{Sx}_a = \mathbf{y}_a$						Compute $\mathbf{x}_b$	
N	NNZ	M_f (GB)	M_p (GB)	T_f (s)	T_s (s)	N	NNZ	M_f (GB)	M_p (GB)	T_f (s)	T_s (s)	T_s (s)	T (days)
807,300	10,368,263	92	26	1747	203	1,017,900	73,841,972	109	2	2070	584	509	~5.1

surrounding the TWOP (see the black dashed line in Figure 10). This results in $41 \times 27 \times 9$ cells in the anomalous subdomain. All unknowns outside this volume are eliminated, and their contributions at the Schur interface are obtained via the Schur complement. Instead of defining the Schur interface as a cuboid, one could have used an irregular body conforming more closely to the TWOP shape. The advantages of using a cuboid are that it is easier to define and that the number of unknowns at the Schur interface is smaller. Note that this choice of anomalous subdomain does not affect the inversion results because one can limit inversion updates to a smaller volume within the cuboid, e.g., to the volume of reservoir.

The previously mentioned anisotropic CSEM inversion over this data set took about 120 iterations; at each iteration, this inversion requires about 432 modeling jobs with different computational transmitter positions and/or orientations per earth resistivity model. Table 2 shows the memory requirements and run time for CSEM modeling using FDFD with and without the Schur complement approach for one frequency (the memory and run time for other frequencies are very similar). This time the number of unknowns in computing the Schur complement is the same as the total number of unknowns in the system. This means that we considered all nodes for computing the Schur complement as opposed to the deepwater Gulf of Mexico example case in which only Schur interface nodes and its close neighbors were chosen from the anomalous nodes,

whereas other interior anomalous nodes were excluded. The reason is that the anomalous subdomain in this case is so small that the full Schur matrix $\mathbf{S}$ occupies relatively little memory anyway.

For each frequency, the standard FDFD method took 10,555 s to factorize the system matrix $\mathbf{M}$ and 1770 s for the backward-forward substitutions to compute CSEM responses for all 432 computational transmitters, whereas the time required to compute the Schur complement $\mathbf{S}$ and intermediate vector $\mathbf{y}$ was, respectively, 11,770 and 724 s, computation of anomalous subdomain fields $\mathbf{x}_a$ by solving the Schur complement system required 773 s to factorize $\mathbf{S}$ and 76 s for the substitutions, and computation of background subdomain fields $\mathbf{x}_b$ required 1687 s. This is a very encouraging result for multimodel simulations, in which the Schur complement approach thus took only $773 + 76 + 1687 = 2536$ s, which is about 20% of the standard FDFD time $(10{,}555 + 1770 = 12{,}325$ s$)$ to simulate CSEM responses for each successive model. Therefore, in the entire CSEM inversion requiring 120 iterations, the total modeling time with the Schur complement approach was only $(11{,}770 + 724 + 120 \times 2536)$ s $= 316{,}814$ s ≈ 3.7 days as compared with standard
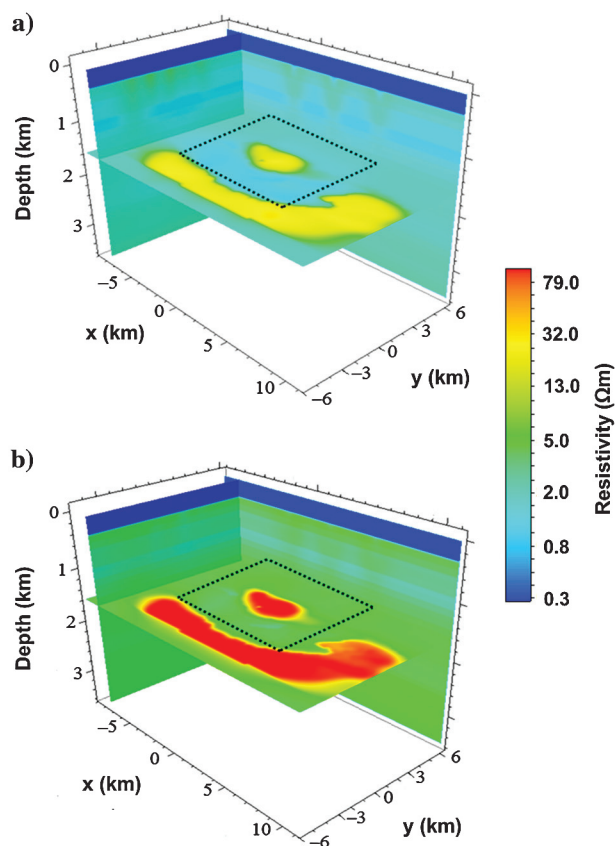
Figure 10. (a) Horizontal and (b) vertical resistivity models from the Troll field area in the North Sea used for synthetic simulations of CSEM responses for the focused inversion case. The black dashed line shows the Schur interface that defines a block of dimension $8 \times 5 \times 0.4$ km^3 containing the TWOP reservoir.
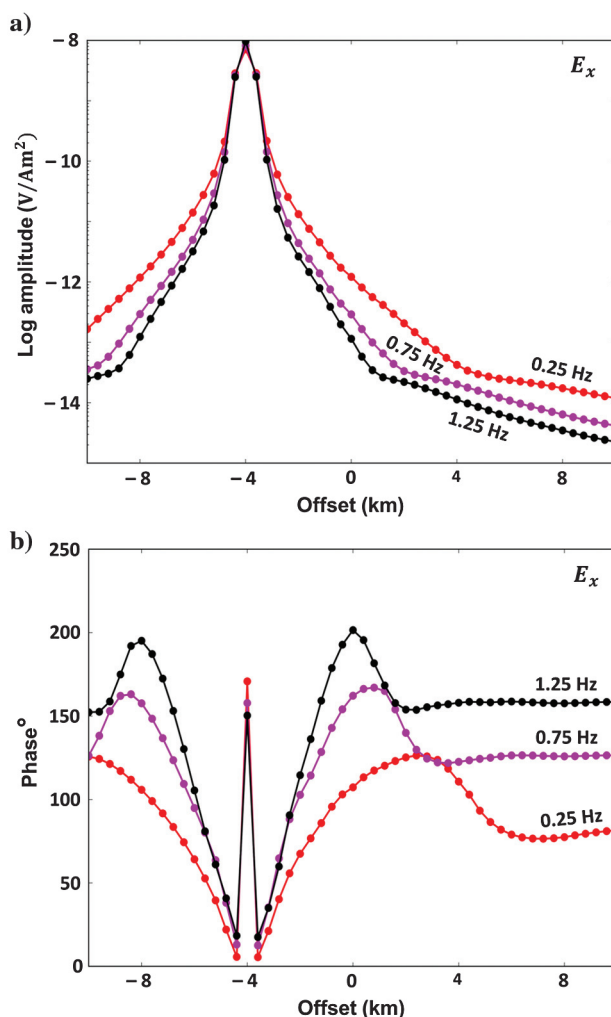
Figure 11. The (a) amplitude and (b) phase responses of the x component of the electric field for the Troll field model (Figure 10) computed using FDFD (solid lines) and FDTD (filled circles) for the frequencies 0.25, 0.75, and 1.25 Hz. The field responses are plotted along a receiver line $y = 3$ km placed on the seabed.

FDFD modeling that took $120 \times 12,325 \text{ s} = 1,479,000 \text{ s} \approx$ 17.1 days. Note that it takes a relatively long time (773 s) to factorize the Schur complement matrix because it has a very dense block corresponding to unknowns located at the Schur interface.

The influence that the number of iterations and the number of transmitters have on the total modeling time is shown in Figure 12. Figure 12a shows a plot of modeling times versus number of iterations while keeping number of transmitters fixed to 432, whereas Figure 12b shows a plot of modeling times versus number of transmitters while keeping number of iterations fixed to 120. For a realistic CSEM inversion, the savings in modeling time can be of up to 70%–80% using the Schur complement approach.

Figures 9 and 12 also indicate that if the number of transmitters is of the order of few thousand, the gain would be reduced to 20%–30% and 40%–50%, respectively, for the Gulf of Mexico and Troll field models. The reason for this reduction is the fact that backward-forward substitutions time would then increase and become comparable with factorization time.

DISCUSSION

We have presented an efficient way of performing multimodel simulations using a Schur complement-based FDFD approach. When used as a forward modeling engine to perform constrained 3D CSEM inversion, it allows for significant run time savings. In the previous section, we demonstrated that one can save up to 35%–40% of the modeling time in the CSEM inversion for deep-water environments when the seawater and air layer resistivities are constrained. We performed similar tests for shallower water: for seawater depth in the range of 800 to 1500 m, the gain turned out to be approximately 20%–30%, which still is considerable. The Troll field example has shown that the gain can be enormous for the focused inversion case — up to 70%–80% of the modeling time in the CSEM inversion depending on the relative sizes of the constrained and unconstrained volumes. If the unconstrained volume is small, the IE method has been considered as the best forward modeling tool for such inversions. Our results demonstrate that similar computational advantage can be achieved also in the framework of FDFD method by using the Schur complement approach.

Another possible application of the Schur complement-based FDFD method is postinversion modeling. Inversion results are non-

unique; there always exists a set of different resistivity models that can explain the measured EM responses. Therefore, one often performs postinversion modeling to test different geologic scenarios, in
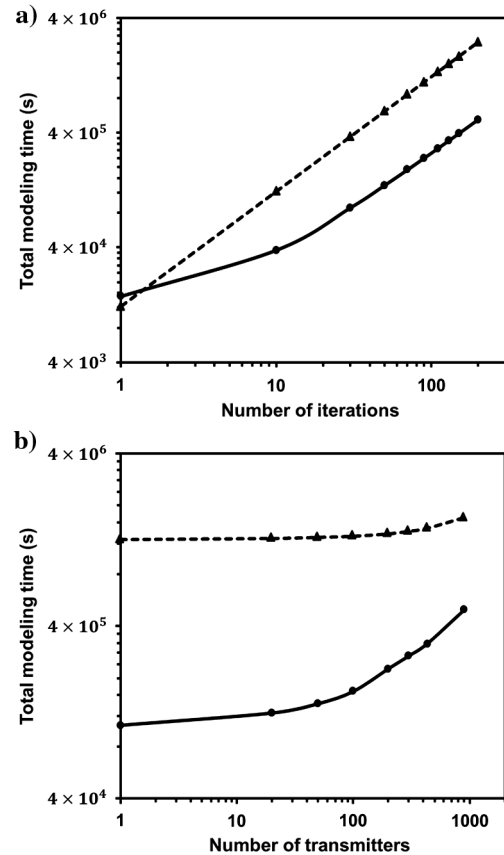

Figure 12. (a) Plots showing the influence of the number of iterations and (b) the number of transmitters on the total modeling times for a CSEM inversion. The Schur complement-based FDFD (solid line) provides a significant reduction of the total modeling time as compared with standard FDFD (dashed line) unless the number of iterations is too small or number of transmitters is too large. The plots were generated using the Troll field model.

Table 2. Memory requirements and observed run time per frequency for performing CSEM modeling with and without the Schur complement approach for the model from the Troll field in Figure 10. CSEM modeling is performed for 432 computational transmitters. The same nomenclature as in Table 1 is used except that the number of RHSs here is 432. The column labeled T (days) shows the projected total modeling time per frequency for a CSEM inversion requiring 120 iterations. Use of the Schur complement-based approach reduces this time by approximately a factor of 5.

		Standard FDFD Modeling				
N	NNZ	M_f (GB)	M_p (GB)	T_f (s)	T_s (s)	T (days)
3,622,500	46,670,460	390	4	10,555	1770	~17.1

		Schur complement-based FDFD modeling										
	Compute **S** by partial factorization of **M**					Compute **y**		Compute $\mathbf{x}_a$ by solving $\mathbf{Sx}_a = \mathbf{y}_a$				Compute $\mathbf{x}_b$	
N	NNZ	M_f (GB)	M_p (GB)	T_f (s)	T_s (s)	N	NNZ	M_f (GB)	M_p (GB)	T_f (s)	T_s (s)	T_s (s)	T (days)
3,622,500	46,670,460	403	20	11,770	724	29,889	64,158,115	59	2	773	76	1687	~3.7

particular, to correct for uncertainties in the thickness and depth placement of the reservoir (Mittet et al., 2008; Fanavoll and Gabrielsen, 2012). Such postinversion modeling also requires many forward modeling jobs in which only a relatively small portion of the model is modified. The use of our Schur complement-based FDFD approach here will certainly allow reducing computational expense.

In our suggested Schur complement approach, we have two matrix equations 5 and 12. It is necessary to use direct solvers to compute the Schur complement $\mathbf{S}$ of the background subdomain by partially factorizing the system matrix $\mathbf{M}$ in equation 5 to be able to reuse the factorization to perform multimodel simulations as explained earlier. The second system of linear equations $\mathbf{S}\mathbf{x}_a = \mathbf{y}_a$ can be solved either by direct or iterative solvers, but only use of direct solvers will allow one to handle multiple RHSs (many EM transmitters) in one run.

As a final remark, note that Tables 1 and 2 show that computing the Schur complement leads to an increased peak memory at one processor. This is related to the fact that the Schur complement matrix $\mathbf{S}$ has a dense block for the Schur interface unknowns and is stored at one host only. To use this approach for a very large Schur interface, one may need to distribute the Schur complement matrix among different computational nodes.

CONCLUSIONS

We have presented an efficient algorithm for fast multimodel 3D CSEM simulations using a Schur complement-based FDFD scheme. This approach takes advantage of the fact that inversion of CSEM data usually requires a large number of modeling jobs on earth models having resistivities that only differ in a limited anomalous subdomain. Although the standard FDFD method would require repeating extensive forward modeling computations on the entire earth model at every inversion iteration, using our Schur complement-based FDFD approach the effect of the subdomain that remains constrained across all earth models can be precomputed once and for all, allowing for significant savings in computational complexity. The results of this paper demonstrate that this approach is extremely valuable for constrained inversions in which the resistivities in a large volume are kept constant throughout the inversion process. In a deepwater setting in which the seawater and air layer are constrained, the savings can amount to up to 35%–40% of the modeling run-time, whereas for an inversion focused on the area occupied by a hydrocarbon reservoir the savings can be even larger: up to 80%.

ACKNOWLEDGMENTS

REFERENCES

Amestoy, P. R., I. S. Duff, J.-Y. L'Excellent, and J. Koster, 2001, A fully asynchronous multifrontal solver using distributed dynamic scheduling: SIAM Journal on Matrix Analysis and Applications, **23**, 15–41, doi: 10.1137/S0895479899358194.

Amestoy, P. R., A. Guermouche, J.-Y. L'Excellent, and S. Pralet, 2006, Hybrid scheduling for the parallel solution of linear systems: Parallel Computing, **32**, 136–156, doi: 10.1016/j.parco.2005.07.004.

Avdeev, D. B., 2005, Three-dimensional electromagnetic modelling and inversion from theory to application: Surveys in Geophysics, **26**, 767–799, doi: 10.1007/s10712-005-1836-x.

Avdeev, D., and S. Knizhnik, 2009, 3D integral equation modeling with a linear dependence on dimensions: Geophysics, **74**, no. 5, F89–F94, doi: 10.1190/1.3190132.

Börner, R. U., 2010, Numerical modeling in geo-electromagnetics: Advances and challenges: Surveys in Geophysics, **31**, 225–245, doi: 10.1007/s10712-009-9087-x.

Da Silva, N. V., L. MacGregor, J. Morgan, M. Warner, and A. Umpleby, 2010, A domain decomposition method for 3-D controlled source electromagnetics: 80th Annual International Meeting, SEG, Expanded Abstracts, 660–664.

Da Silva, N. V., J. V. Morgan, L. Macgregor, and M. Warner, 2012, A finite element multifrontal method for 3D CSEM modeling in the frequency-domain: Geophysics, **77**, no. 2, E101–E115, doi: 10.1190/geo2010-0398.1.

Davydycheva, S., V. Druskin, and T. Habashy, 2003, An efficient finite difference scheme for electromagnetic logging in 3D anisotropic inhomogeneous media: Geophysics, **68**, 1525–1536, doi: 10.1190/1.1620626.

Duff, I., A. Erisman, and J. Reid, 1986, Direct methods for sparse matrices: Oxford University Press.

Endo, M., X. Liu, and M. S. Zhdanov, 2010, Hybrid method for 3D modeling of electromagnetic fields in complex structures with inhomogeneous background conductivity: 80th Annual International Meeting, SEG, Expanded Abstracts, 753–757.

Fanavoll, S., S. Ellingsrud, P. T. Gabrielsen, R. Tharimela, and D. Ridyard, 2012, Exploration with the use of EM data in the Barents Sea: The potential and the challenges: First Break, **30**, 89–96.

Fanavoll, S., and P. T. Gabrielsen, 2012, Integrated interpretation of a CSEM anomaly on the Nordland ridge, Norwegian continental shelf: 82nd Annual International Meeting, SEG, Expanded Abstracts, doi: 10.1190/segam2012-0430.1.

Gabrielsen, P. T., P. Abrahamson, M. Panzner, S. Fanavoll, and S. Ellingsrud, 2013, Exploring frontier areas using 2D seismic and 3D CSEM data, as exemplified by multi-client data over the Skrugard and Havis discoveries: First Break, **31**, 63–71.

Gabrielsen, P. T., I. Brevik, R. Mittet, and L. O. Løseth, 2009, Investigating the exploration potential for 3D CSEM using a calibration survey over the Troll field: First Break, **27**, 67–75.

Gabrielsen, P. T., D. V. Shantsev, and S. Fanavoll, 2012, 3D CSEM for hydrocarbon exploration in the Barents Sea: 5th Saint Petersburg International Conference and Exhibition, EAGE, Extended Abstracts, C002.

Grayver, A. V., R. Streich, and O. Ritter, 2013, Three-dimensional parallel distributed inversion of CSEM data using a direct forward solver: Geophysical Journal International, **193**, 1432–1446, doi: 10.1093/gji/ggt055.

Gupta, P. K., L. A. Bennett, and A. P. Raiche, 1987, Hybrid calculations of the three-dimensional electromagnetic response of buried conductors: Geophysics, **52**, 301–306, doi: 10.1190/1.1442304.

Hamilton, M. P., G. Mikkelsen, R. Poujardieu, and A. Price, 2010, CSEM survey over the Frigg gas field, North Sea: 72nd Annual International Conference and Exhibition, EAGE, Extended Abstract, P074.

Haynsworth, E. V., 1968, On the Schur complement: Basel Mathematical Notes, University of Basel, BMN 20.

Kanhalangsy, C., N. Golubev, J. J. Zach, and D. Baltar, 2011, Anisotropic CSEM inversion near the "Tiger" well in AC 818, Gulf of Mexico: 81st Annual International Meeting, SEG, Expanded Abstracts, 609–613.

Liu, J., 1992, The multifrontal method for sparse matrix solution: Theory and practice: SIAM Review, **34**, 82–109, doi: 10.1137/1034004.

Løseth, L. O., and B. Ursin, 2007, Electromagnetic fields in planarly layered anisotropic media: Geophysical Journal International, **170**, 44–80, doi: 10.1111/j.1365-246X.2007.03390.x.

Lu, Y., and C. Y. Shen, 1997, A domain decomposition finite-difference method for parallel numerical implementation of time-dependent Maxwell's equations: IEEE Transactions on Antennas and Propagation, **45**, 556–562, doi: 10.1109/8.558671.

Maaø, F. A., 2007, Fast finite-difference time-domain modeling for marine-subsurface electromagnetic problems: Geophysics, **72**, no. 2, A19–A23, doi: 10.1190/1.2434781.

Mikkelsen, J. K., T. Norheim, and S. I. Sagatun, 2005, The Troll story: Presented at Offshore Technology Conference, 17108.

Mittet, R., 2010, High-order finite-difference simulation of marine CSEM survey using a corresponding principle for wave and diffusion fields: Geophysics, **75**, no. 1, F33–F50, doi: 10.1190/1.3278525.

Mittet, R., K. Brauti, H. Maulana, and T. A. Wicklund, 2008, CMP inversion and post-inversion modelling for marine CSEM data: First Break, **26**, 59–67.

Morten, J. P., F. Roth, S. A. Karlsen, D. Timko, C. Pacurar, P. A. Olsen, A. K. Nguyen, and J. Gjengedal, 2012, Field appraisal and accurate resource estimation from 3D quantitative interpretation of seismic and CSEM data: The Leading Edge, **31**, 447–456, doi: 10.1190/tle31040447.1.

Newman, G. A., and D. L. Alumbaugh, 1995, Frequency-domain modeling of airborne electromagnetic responses using staggered finite differences: Geophysical Prospecting, **43**, 1021–1042, doi: 10.1111/j.1365-2478.1995.tb00294.x.

Roth, F., J. E. Lie, M. Panzner, and P. T. Gabrielsen, 2013, Improved target imaging with a high-power deck-mounted CSEM source — A field example from the North Sea: 75th Annual International Conference and Exhibition, EAGE, Extended Abstracts, Tu1110.

Saad, Y., 2003, Iterative methods for sparse linear systems: SIAM.

Schwarzbach, C., and E. Haber, 2013, Finite element based inversion for time-harmonic electromagnetic problems: Geophysical Journal International, **193**, 615–634, doi: 10.1093/gji/ggt006.

Smith, B. F., P. E. Bjørstad, and W. Gropp, 1996, Domain decomposition: Parallel multilevel methods for elliptic partial differential equations: Cambridge University Press.

Smith, J. T., 1996, Conservative modeling of 3-D electromagnetic fields, Part II: Biconjugate gradient solution and an accelerator: Geophysics, **61**, 1319–1324, doi: 10.1190/1.1444055.

Sourbier, F., A. Haidar, L. Giraud, H. Ben-Hadj-Ali, S. Operto, and J. Virieux, 2011, Three-dimensional parallel frequency-domain visco-acoustic wave modelling based on a hybrid direct/iterative solver: Geophysical Prospecting, **59**, 834–856.

Streich, R., 2009, 3D finite-difference frequency-domain modeling of controlled-source electromagnetic data: Direct solution and optimization for high accuracy: Geophysics, **74**, no. 5, F95–F105, doi: 10.1190/1.3196241.

Taflove, A., and S. C. Hagness, 2005, The finite-difference time domain method: Artech House.

Yang, D., and D. W. Oldenburg, 2012, Three-dimensional inversion of airborne time-domain electromagnetic data with applications to a porphyry deposit: Geophysics, **77**, no. 2, B23–B34, doi: 10.1190/geo2011-0194.1.

Yee, K., 1966, Numerical solution of initial boundary value problems involving Maxwell's equations in isotropic media: IEEE Transactions on Antennas and Propagation, **14**, 302–307, doi: 10.1109/TAP.1966.1138693.

Zach, J. J., A. K. Bjørke, T. Støren, and F. Maaø, 2008, 3D inversion of marine CSEM data using a fast finite-difference time-domain forward code and approximate Hessian-based optimization: 78th Annual International Meeting, SEG, Expanded Abstracts, 614–618.

Zaslavsky, M., V. Druskin, S. Davydycheva, L. Knizhnerman, A. Abubakar, and T. Habashy, 2011, Hybrid finite-difference integral equation solver for 3D frequency domain anisotropic electromagnetic problems: Geophysics, **76**, no. 2, F123–F137, doi: 10.1190/1.3552595.

Zhang, F., 2005, The Schur complement and its applications: Springer.

Zhdanov, M. S., 2009, Geophysical electromagnetic theory and methods: Elsevier.